

## Supporting Information

### Highly active and durable carbon nitride fibers as metal-free bifunctional oxygen electrodes for flexible Zn–air batteries

Sambhaji S. Shinde, Jin-Young Yu, Jae-Won Song, Yoon-Ho Nam, Dong-Hyung Kim, Jung-Ho Lee\*

*Department of Materials and Chemical Engineering, Hanyang University, Ansan, Kyunggido, 426-791, Republic of Korea*

*E-mail: jungho@hanyang.ac.kr*

## Experimental Methods

### Chemicals and Materials

Melamine monomer, L-alanine, L-cysteine, O-phospho-L-serine, aqueous ammonia, Nafion-117 solution, acetone, sulfuric acid, hydrogen peroxide, platinum(II) acetylacetonate, ethylene glycol (Sigma-Aldrich), carbon cloth (Spectracarb 2040-A, Fuel Cell Store), and Zn plate (Sigma-Aldrich) were employed as received.

### Carbon cloth pretreatment

Carbon cloth was consecutively washed with acetone, H<sub>2</sub>SO<sub>4</sub> (1 M), and DI water under sonication for 2 h in each solution to thoroughly remove organic residues and other impurities. The treated carbon cloth was then soaked overnight in piranha solution (i.e., a 3:1 by volume mixture of concentrated H<sub>2</sub>SO<sub>4</sub> and 30% H<sub>2</sub>O<sub>2</sub>) to enhance its hydrophilicity. The resulting carbon cloth was washed with DI water several times. Finally, the cleaned carbon cloth was stored in DI water to avoid regaining hydrophobicity.

### In situ growth of phosphorus and sulfur co-doped carbon nitride nanofibers (PS-CNF) on carbon cloth

Melamine, L-alanine, L-cysteine, and O-phospho-L-serine were dissolved in 20 ml ethylene glycol at the mass ratio of 1:0.5:0.2:0.2 under vigorous stirring. Subsequently, a 60 ml solution of 0.2 M HNO<sub>3</sub> was mixed under supersonic stirring in an ice bath, followed by addition of a few drops of aqueous ammonia. The resulting solution was vigorously stirred for 10 min at room temperature. The pretreated carbon cloth was immersed into the reaction mixture and heated at 80 °C for 1 h to allow in situ fiber growth. After cooling, the fiber-coated cloth was washed with DI water several times, and then heated in a quartz container at 300 °C for 2 h under N<sub>2</sub> flow. For comparison, pristine carbon nitride fibers were also

prepared using the same procedure, except the L-cysteine, and O-phospho-L-serine. The mass loading of PS-CNF on carbon cloth was  $\sim 0.20 \text{ mg cm}^{-2}$ .

### **Synthesis of Pt/C on carbon cloth**

Oleic acid (0.2 ml), oleylamine (0.2 ml), 1,2-hexadecanediol (43 mg), and phenyl ether (10 ml) were mixed in a round bottom flask under stirring and heated at  $120 \text{ }^\circ\text{C}$  for 30 min. Platinum(II) acetylacetonate was then mixed into this reaction solution. Pretreated carbon cloth was immersed in the reaction solution and heated at  $65 \text{ }^\circ\text{C}$  for 30 min. Finally, prepared carbon cloth was washed and dried at  $200 \text{ }^\circ\text{C}$  for 1 h under  $\text{N}_2$  flow, and then cooled to room temperature. The concentration of platinum acetylacetonate was controlled to give the Pt loading of  $\sim 0.20 \text{ mg cm}^{-2}$ , similar to the mass loading of the PS-CNF on carbon cloth.

### **Materials characterization**

Surface structure and morphology were examined by means of field-emission scanning electron microscopy (FESEM; JEOL-6700F). Transmission electron microscopy (TEM) energy dispersive X-ray spectroscopy (EDS) elemental mapping images were acquired using a JEOL JEM-2010 instrument. X-ray photoelectron spectra (XPS) were acquired using an XPS spectrometer (VG Scienta R3000) equipped with an Al  $K\alpha$  source ( $1486.6 \text{ eV}$ ). The  $\text{N}_2$  sorption isotherms measured on an AUTOSORB-1-MP system at  $77 \text{ K}$ , after the samples were degassed in a vacuum at  $120 \text{ }^\circ\text{C}$  for 12 h. The specific surface areas and pore size distribution were investigated by Brunauer–Emmett–Teller (BET) and Barrett, Joyner, and Halenda (BJH) methods, respectively. X-ray diffraction (XRD) patterns were analyzed via a Rigaku D/MAX-2500 X-ray diffractometer (Cu  $K\alpha$ ,  $\lambda = 1.5406 \text{ \AA}$ ). Fourier transform infrared spectra were acquired using a PerkinElmer Spectrum GX instrument. Raman spectra were produced on RM 1000 (Ranishaw, UK) spectrometer. The elemental analysis (EA) was performed by inductively coupled plasma (ICP) emission spectroscopy on a Thermo Jarrell-Ash ICP-9000 (N + M) spectrometer, and by a WS-CHN800 elemental analyzer.

### **Electrochemical measurements**

Electrochemical tests were performed using an electrochemical workstation (CHI 760 D, CH Instruments, Inc., USA). The electrochemical activities of the catalysts were measured using a standard three-electrode electrochemical cell filled with  $0.1 \text{ M KOH}$  electrolyte. The as-prepared PS-CNFs on carbon cloth were used directly as the working electrode for

electrochemical characterizations. Pt wire and an Ag/AgCl electrode (saturated with KCl) were used as the counter and reference electrodes, respectively. Electrochemical impedance spectroscopy measurements were conducted over the frequency range of 1 MHz–0.01 Hz with the amplitude of 5 mV. The current density was normalized to the geometrical surface area, and the measured potentials vs. Ag/AgCl were converted to a reversible hydrogen electrode (RHE) scale according to the Nernst equation ( $E_{\text{RHE}} = E_{\text{Ag/AgCl}} + 0.205 + 0.059 \times \text{pH}$ ). A flow of O<sub>2</sub> was maintained over the electrolyte during the measurement to ensure its continued O<sub>2</sub> saturation. Polarization data were measured using linear sweep voltammetry conducted at a scan rate of 5 mV s<sup>-1</sup> with automatic iR compensation.

The electron transfer number (*n*) for the ORR process was calculated using the Koutecky–Levich equation<sup>S1</sup>:

$$\frac{1}{J} = \frac{1}{J_K} + \frac{1}{B\omega^{1/2}}$$

$$B = 0.2nFC_O(D_O)^{2/3}\nu^{-1/6},$$

where *J* is the measured current, *J<sub>K</sub>* is the kinetic current,  $\omega$  is the electrode rotation rate in rpm, *F* is the Faraday constant (96485 C mol<sup>-1</sup>), *C<sub>O</sub>* is the bulk concentration of O<sub>2</sub> (1.2 × 10<sup>-6</sup> mol cm<sup>-3</sup>), *D<sub>O</sub>* is the diffusion coefficient of O<sub>2</sub> (1.9 × 10<sup>-5</sup> cm<sup>2</sup> s<sup>-1</sup>), and  $\nu$  is the kinematic viscosity of the electrolyte (0.01 cm<sup>2</sup> s<sup>-1</sup>). The constant 0.2 is adopted when the rotation speed is expressed in rpm. The peroxide yields (HO<sub>2</sub><sup>-</sup>) and number of transferred electrons (*n*) were calculated using the equations below:

$$H_2O_2^- (\%) = 100 \frac{2I_r/N}{I_d + I_r/N}$$

$$n = 4 \frac{I_d}{I_d + I_r/N},$$

where *I<sub>d</sub>* is the disk current, *I<sub>r</sub>* is the ring current, and *N* the is current collection efficiency of the Pt ring; *N* was determined to be 0.40.

### Zn–air battery performance

For the Zn–air battery test, as-prepared PS-CNF on carbon cloth was used as air cathode material, 6 M KOH was used as the electrolyte, and a polished zinc plate was utilized as the anode unless otherwise stated. Both electrodes were assembled into a lab-made Zn–air battery. A similar process was utilized to investigate the performance of a three-electrode

rechargeable Zn–air battery; the prepared air electrodes had the mass ratio of 1:1 for the ORR and OER electrodes.

### **Flexible Zn–air battery assembly**

First, a polymer hydrogel electrolyte was prepared according to the procedure below. Under vigorous stirring, 5 g of polyvinyl alcohol (PVA) and 0.1 g of polyethylene oxide (PEO) were mixed into 50 ml of KOH solution (0.1 M) containing 0.02 M zinc oxide under vigorous stirring at 95 °C. The resultant uniform solution was poured onto a glass substrate to yield a thin film, frozen for 12 h at –3 °C, and then held at room temperature and atmospheric pressure to allow it to soften. To assemble a robust PVA gel layer, we repeated this procedure 2–3 times. Finally, polished Zn foil (0.05 mm thick) and PS-CNF grown in situ on carbon cloth were placed on opposite sides of the PVA gel layer as the anode and cathode. Next, assembly with polymer and aluminum packaging was conducted by using a packing machine.

## RESULTS AND DISCUSSION

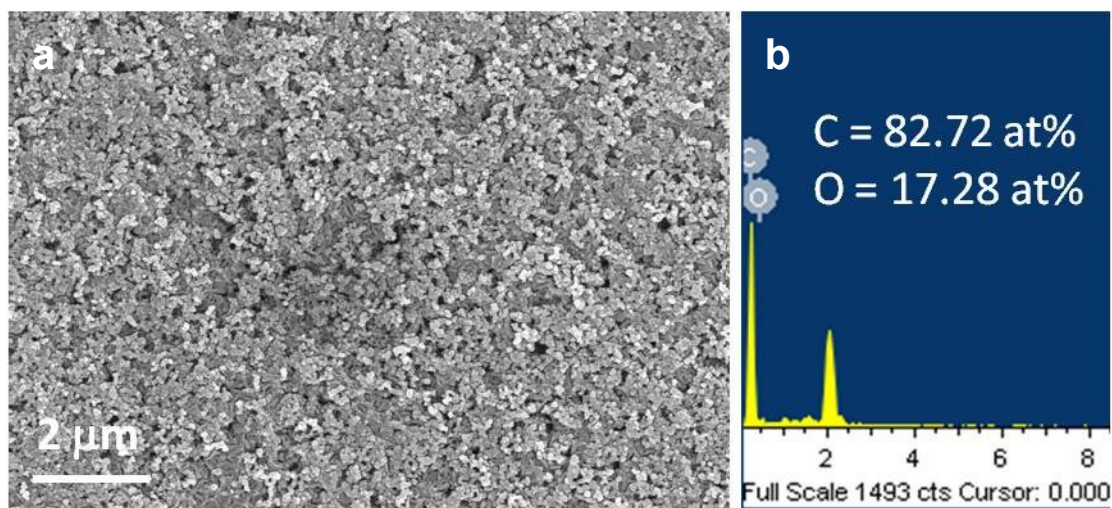


**Figure S1.** (a) Scanning electron micrograph of pretreated carbon cloth; (b) corresponding EDS spectrum, confirming the absence of any other organic or metal impurities.

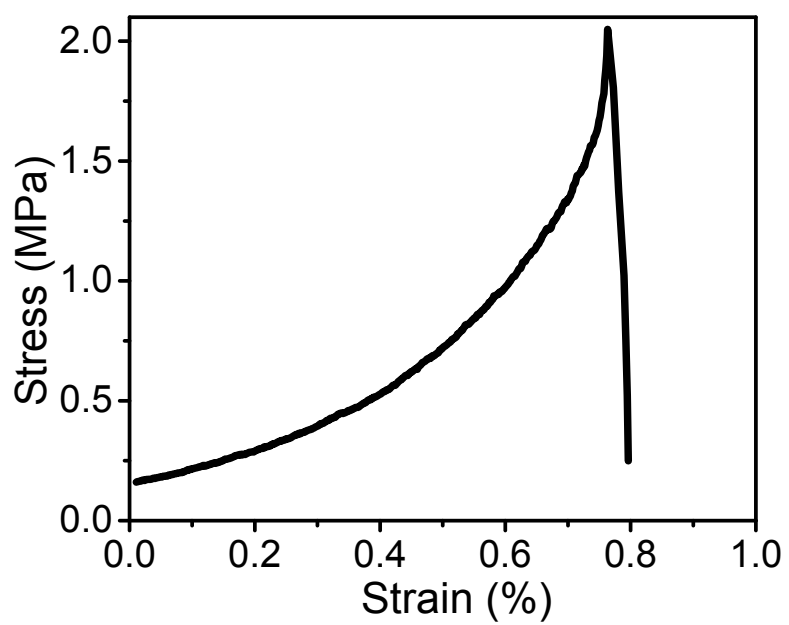


**Figure S2.** Stress–strain analysis of the PS-CNF catalyst.

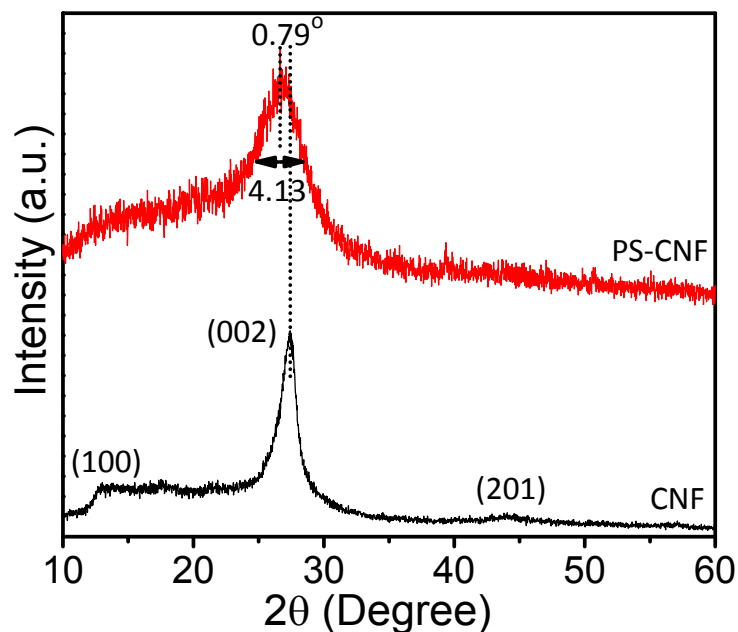


**Figure S3.** X-ray diffraction patterns of pristine CNF and PS-CNF catalysts.

The graphitic structural features of prepared 3D CNF and PS-CNF were confirmed by means of XRD analysis. The presence of graphitic carbon nitride domains was determined by the appearance of two signals in the XRD patterns (Figure S3). Namely, the strong orientation observed at  $26.65^\circ$  ( $d = 0.332$  nm) was assigned to (002) interlayer diffraction of the graphitic C–N structure and the small shoulder at  $12.86^\circ$  was attributed to the (100) interlayer spacing ( $d = 0.665$  nm) of in-planar repetitive tri-*s*-triazine units.<sup>S2</sup> Remarkably, the characteristic (002) peak of PS-CNS was hypsochromically shifted by  $0.79^\circ$  and considerably broadened by  $4.13^\circ$  compared to that of CNF. The relatively weak intensity of PS-CNF compared to that of pristine CNF shows its defect-rich nature, thereby confirming that the proposed design strategy is successful in the fabrication of carbon nitride nanofibers co-doped with phosphorus and sulfur.

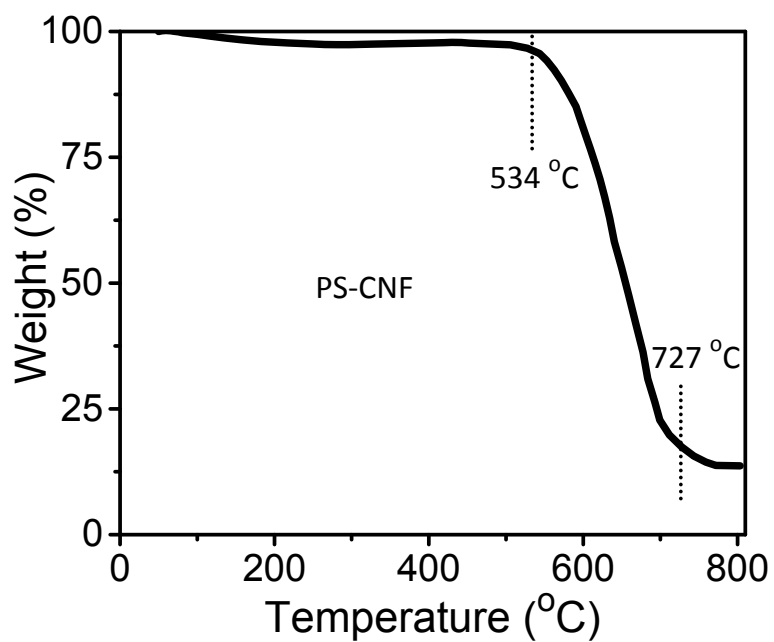


**Figure S4.** Thermogravimetric curve of PS-CNF hybrid catalyst. The PS-CNF was found to be stable up to ~530 °C, demonstrating its thermally stable construction from triazine units in the catalysts. However, PS-CNF slowly crumbles upon elevating temperature above 530 °C enlightening a superior thermal stability.

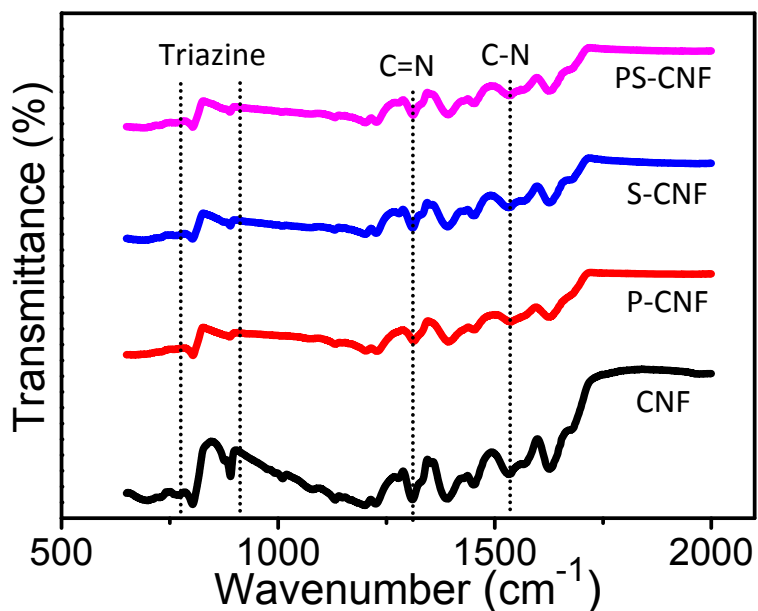


**Figure S5.** Fourier transform infrared spectra of as-prepared pristine CNF, P-CNF, S-CNF, and PS-CNF catalysts.

The in situ growth of PS-CNF on carbon cloth was confirmed by means of Fourier transform infrared spectroscopy (Figure S5). The characteristic absorption modes observed in the regions of 700–920 and 1200–1700  $\text{cm}^{-1}$  were respectively assigned to the breathing modes of triazine units and the stretching modes of C–N heterocycles.<sup>S3</sup> The apparent shifting and reduction in intensity of absorption modes compared to that of pristine CNF verifies the heteroatom doping. Further, an additional mode observed at 1075  $\text{cm}^{-1}$  was assigned to the P–N stretching mode.<sup>S4</sup> The peak observed at 1309  $\text{cm}^{-1}$  was assigned to the C=N stretching mode, in good agreement with XPS results. The aromatic ring modes of graphitic C–N were also observed at 1536  $\text{cm}^{-1}$ . This facile strategy is promising for the synthesis of flexible, large-scale, nanostructured polymeric carbon nitride structures on carbon cloth, as well consistent with XRD, EDS, and XPS analyses.

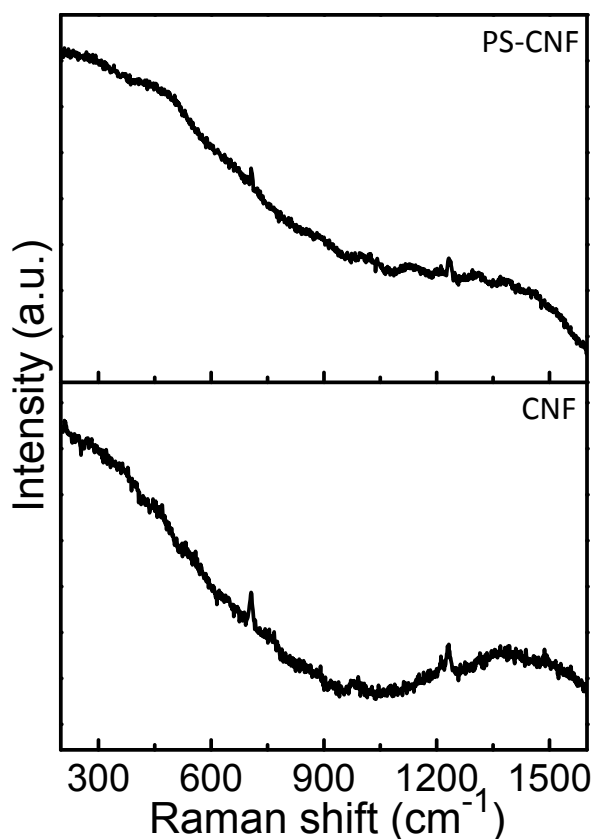


**Figure S6.** Raman spectra of the CNF and PS-CNF catalysts. Raman spectra of CNF and PS-CNF showed the peaks at 707 and 1232  $\text{cm}^{-1}$  illustrating the presence of ring breathing modes of tri-s-triazine (i.e., C-N vibrations).<sup>S4</sup> In case of PS-CNF, the additional broadened weak shoulders are also observed at 1125, 1305, and 1376  $\text{cm}^{-1}$ . The weak peak at 983 and 1010  $\text{cm}^{-1}$  in CNF and PS-CNF are originated from the out-of-plane vibrations of C-C.<sup>S5</sup> This feature manifests a similar crystal structure of prepared CNF-based catalysts, which are consistent with XRD and FTIR results.

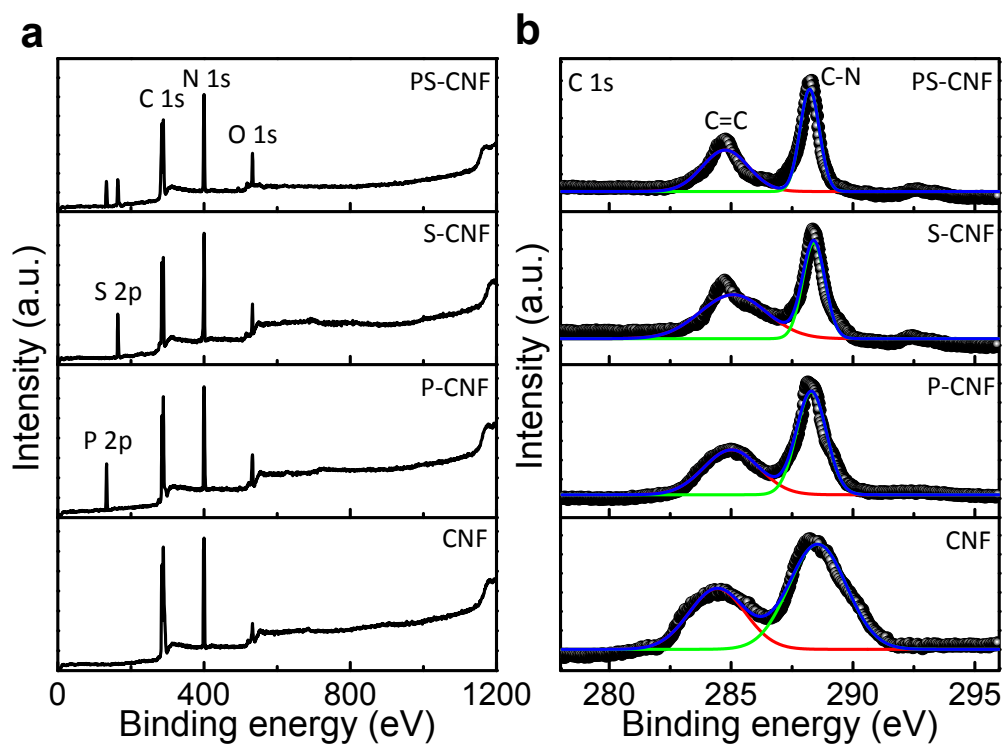


**Figure S7.** (a) XPS survey scan spectra and (b) curve-fitted high-resolution C 1s XPS spectra of pristine CNF, P-CNF, S-CNF, and PS-CNF catalysts.

It did not show any metal-related or other impurity-related signals, verifying that the prepared carbon nitride fibers (CNFs) were completely metal-free catalysts. The C 1s spectra of pristine CNF, P-CNF, S-CNF, and PS-CNF catalysts each showed two peaks at 284.8 and 288.2 eV. The former is recognized as the graphitic C=C reference carbon, whereas the latter is attributed to  $sp^2$ -bonded C in  $N=C(-N)_2$ .<sup>S7</sup>

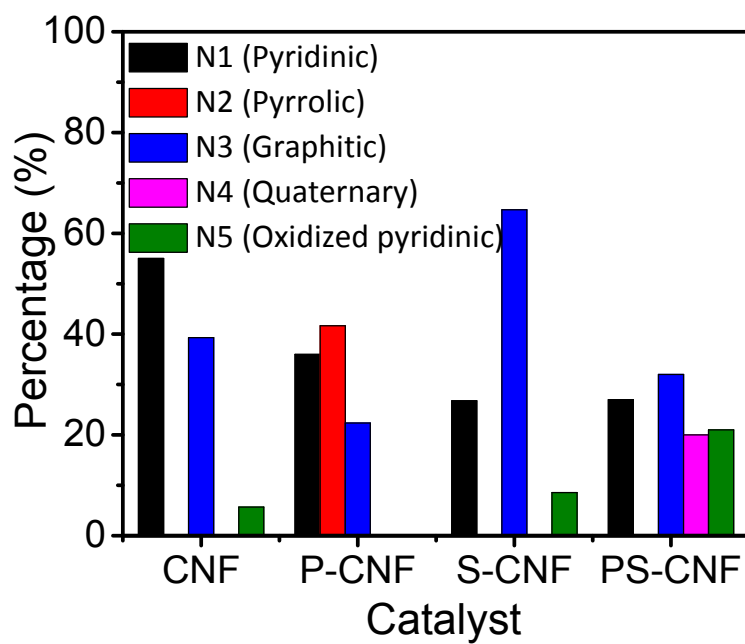


**Figure S8.** Quantification of the types of nitrogen in terms of relative percentages of total nitrogen content in pristine CNF, P-CNF, S-CNF, and PS-CNF catalysts.

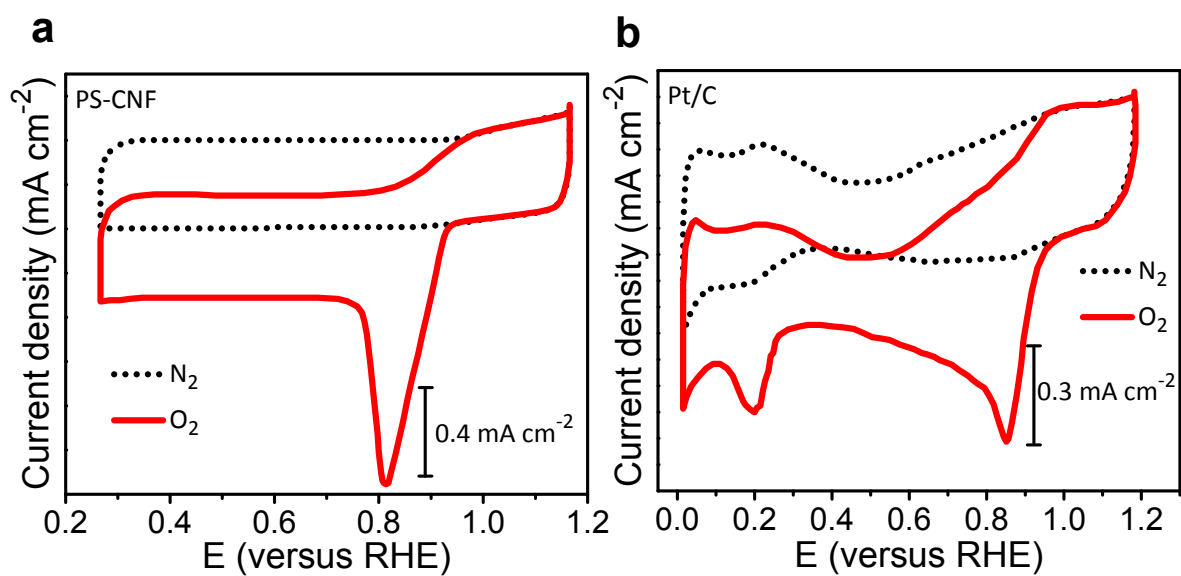


**Figure S9.** Cyclic voltammograms of (a) PS-CNF and (b) reference Pt/C catalysts in N<sub>2</sub>- and O<sub>2</sub>-saturated 0.1 M aqueous KOH electrolyte solutions.

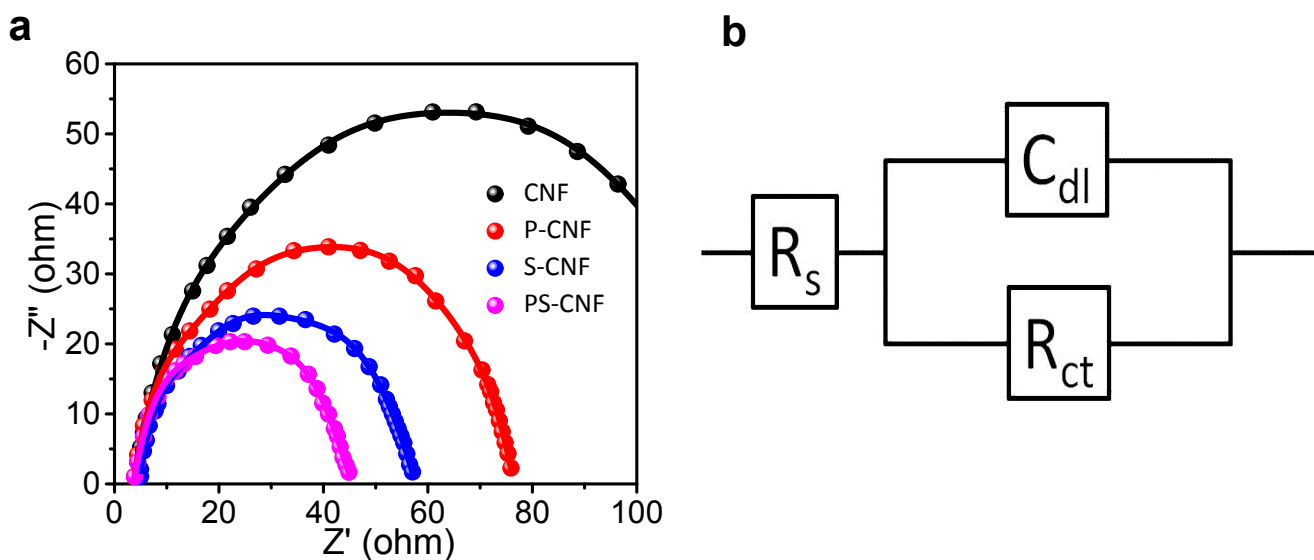


**Figure S10.** (a) Electrochemical impedance spectra (EIS) of pristine CNF, P-CNF, S-CNF, and PS-CNF catalysts at  $-0.2$  V vs. RHE in 0.1 M KOH; (b) corresponding equivalent circuit. The EIS semicircular diameter measured for PS-CNF was much smaller than those of CNF, P-CNF, and S-CNF, indicating smaller contact and charge transfer impedance arising from the synergy between co-dopants P and S, which were highly advantageous for electrochemical reactions.

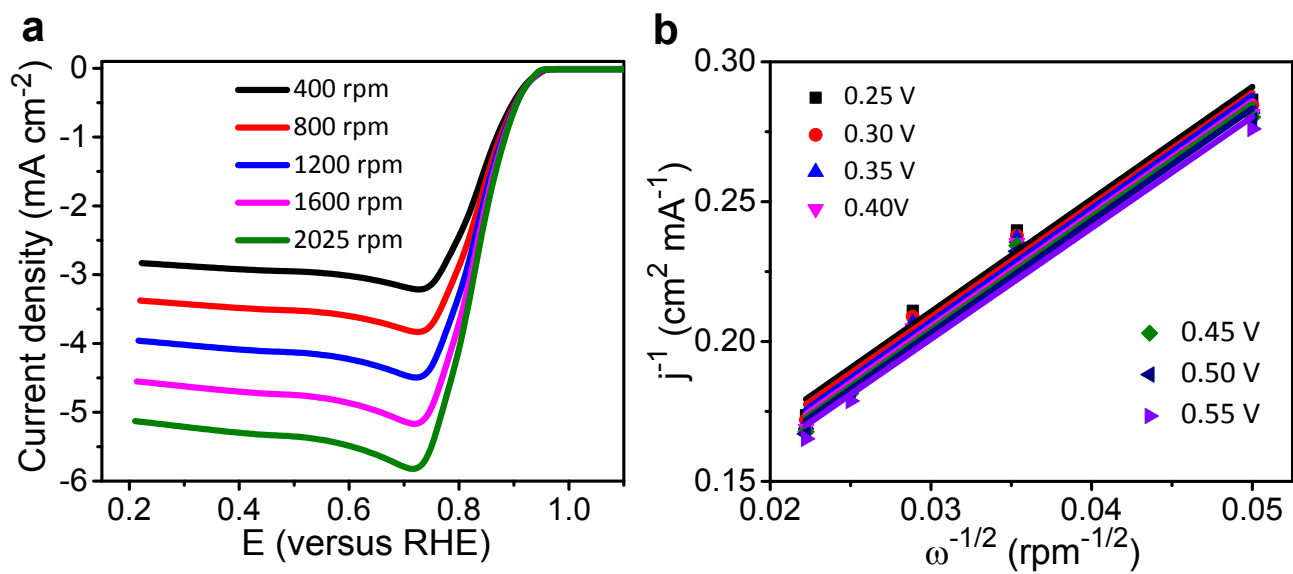


**Figure S11.** (a) LSV polarization curves of Pt/C for ORR on RDE, acquired under various rotating speeds; (b) corresponding Koutecky–Levich plots for various potentials.

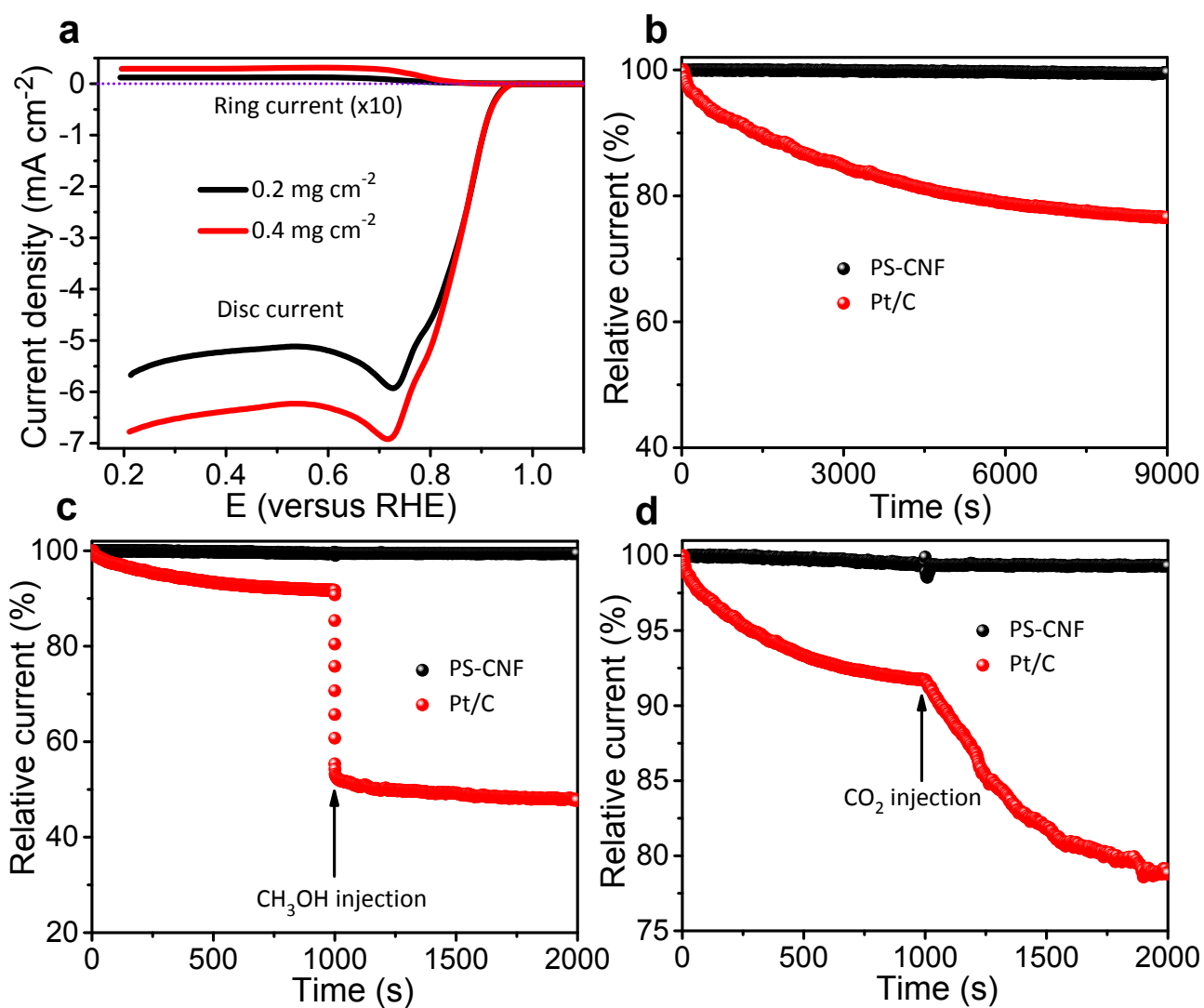


**Figure S12.** (a) RRDE measurements (1600 rpm) of the ORR over PS-CNF catalysts having various catalyst mass loadings. (b) ORR chronoamperometric response of PS-CNF and Pt/C in O<sub>2</sub>-saturated 0.1 M KOH. (c) Chronoamperometric responses in O<sub>2</sub>-saturated 0.1 M KOH over PS-CNF and Pt/C catalysts, before and after injection of CH<sub>3</sub>OH (2 M). (d) CO poisoning tests.

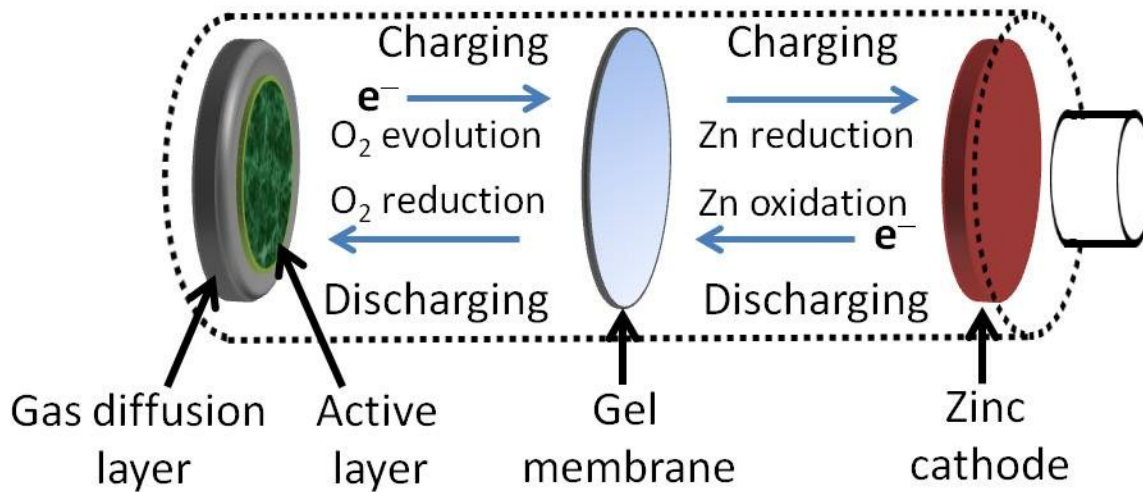


**Figure S13.** Schematic representation of primary Zn–air battery.

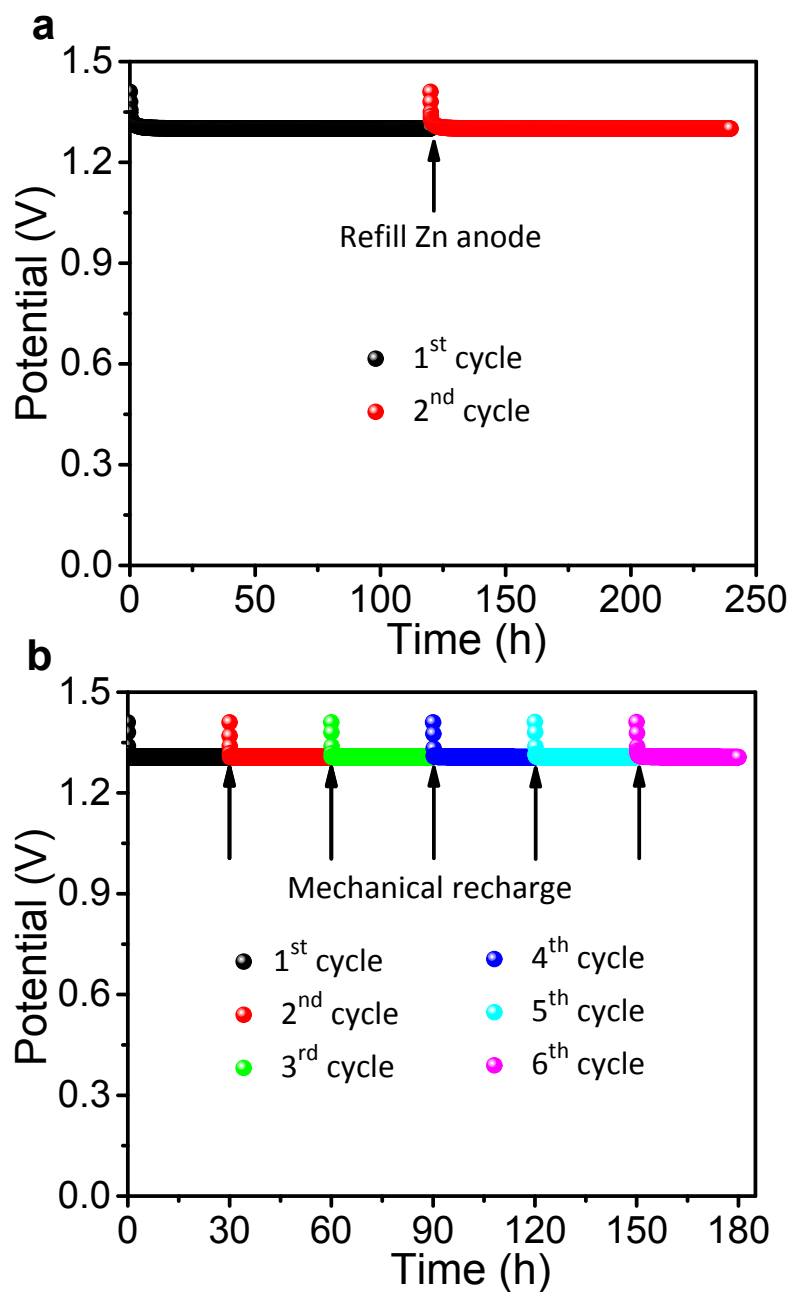


**Figure S14.** (a) Long life durability (mechanical rechargeable) for the primary Zn–air battery with PS-CNF as the air cathode under discharge at the current density of  $2 \text{ mA cm}^{-2}$  (2 cycles). (b) Mechanical recharging for 6 possible cycles. The battery was mechanically rechargeable.

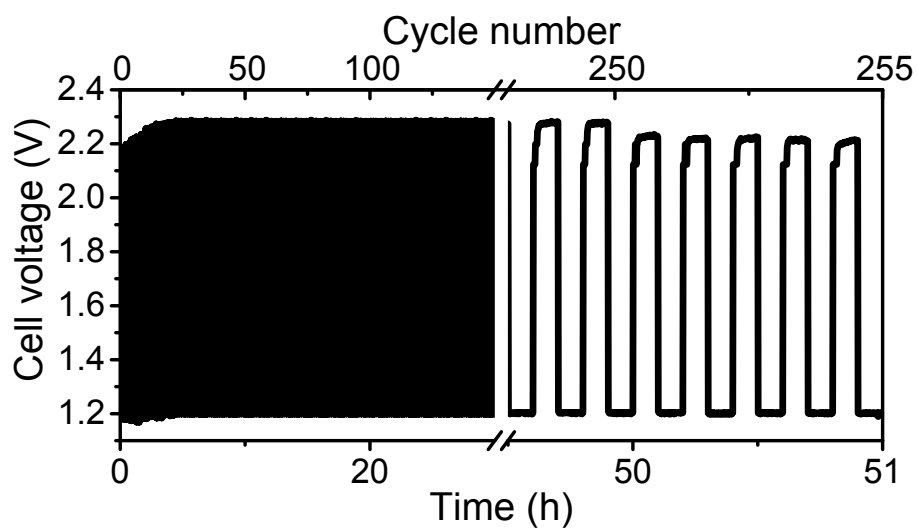


**Figure S15.** Charge/discharge cycling curves of a three-electrode Zn-air battery using Pt/C and IrO<sub>2</sub> as ORR and OER catalysts, respectively, in 6 M KOH electrolyte.

## Supplementary tables

**Table S1.** Elemental compositions and electrical conductivities of the prepared CNF, P-CNF, S-CNF, and PS-CNF catalysts.

Sample	C (%)	N (%)	P (%)	S (%)	O (%)	Conductivity (S m <sup>-1</sup> )
CNF	44.04	52.51	-	-	3.45	52
P-CNF	40.32	48.69	6.97	-	4.02	86
S-CNF	40.48	48.26	-	7.05	4.21	113
PS-CNF	40.21	48.34	3.38	3.61	4.46	165

**Table S2.** Various nitrogen moieties as designated for the pristine CNF, P-CNF, S-CNF, and PS-CNF catalysts: N1 (pyridinic), N2 (pyrrolic), N3 (graphitic), N4 (quaternary) and N5 (pyridinic N<sup>+</sup>O<sup>-</sup>). Note that quaternary N can induce non-uniform electron density distributions on adjacent carbon atoms and facilitate O<sub>2</sub> adsorption and dissociation, thereby functioning as an efficient active site for the ORR.

Sample	N1 (%)	N2 (%)	N3 (%)	N4 (%)	N5 (%)
CNF	398.69	-	400.01	-	402.03
P-CNF	397.97	399.43	400.51	-	-
S-CNF	398.66	-	400.33	-	403.18
PS-CNF	398.63	-	400.01	401.31	402.36

**Table S3.** Electrocatalytic performance metrics of recently reported efficient bifunctional electrocatalysts toward ORR/OER.

Catalyst	Loading (mg cm <sup>-2</sup> )	ORR onset potential (V vs. RHE)	ORR Tafel slope (mV dec <sup>-1</sup> )	ORR half-wave potential (E <sub>1/2</sub> ) (V vs. RHE)	OER onset potential (V vs. RHE)	OER Tafel slope (mV dec <sup>-1</sup> )	OER potential @ 10 mA cm <sup>-2</sup> (E <sub>j=10</sub> ) (V vs. RHE)	Overall oxygen electrode activity ΔE (E <sub>j=10</sub> - E <sub>1/2</sub> ) (V)	Reference
PS-CNF	0.2	0.95	29	0.86	1.32	89	1.55	0.69	This work
NCNF-1000	0.1	0.94		0.85	1.30		1.84	1.02	S8
NPMC-1000	0.15	0.94	-	0.85	1.30	-	-	-	S9
P,S-CNS	0.15	0.97	61	0.87	1.26	64	1.56	0.69	S10
N-GRW	0.6	0.92	50	0.84	1.53	62	1.66	0.82	S11
NiO/CoN	0.2	0.89	-	0.68	1.47	35	1.53	0.85	S12
PCN-CFP	0.20	0.94	122.3	0.67	1.53	61.6	1.63	0.96	S13
CoO/N-G	0.7	0.90	48	0.81	1.30	71	1.57	0.76	S14
Fe@NC	0.31	0.96	-	0.83	1.52	-	1.71	0.88	S15
Mn <sub>x</sub> O <sub>y</sub> /N-C	0.21	0.85	-	0.81	1.55	82.6	1.68	0.87	S16
N-G/CNT	0.25	0.88	-	0.63	1.50	83	1.63	1.00	S17

**Table S4.** Performance metrics of primary Zn–air batteries based upon various electrocatalysts.

Catalyst	OCP (V)	Power density (mW cm <sup>-2</sup> )	Specific capacity (mA h g <sup>-1</sup> )	Durability (h)	Reference
PS-CNF	1.49	231	698	240 (1.31 V)	This work
NCNF-1000	1.48	185	378	83 (1.25 V)	S8
NPMC-1000	1.48	55	735	240 (~1.3 V)	S9
P,S-CNS	1.51	198	830	210 (~1.3 V)	S10
N-GRW	1.46	65	873	30 (~1.0 V)	S11
NiO/CoN	1.46	79.6	690	-	S12
NiC <sub>2</sub> O <sub>4</sub>	-	-	580	10 (~1.25 V)	S18
CoO/N-CNT	1.4	265	570	-	S19
FePc-Py-CNTs	-	-	-	100 (~1.2 V)	S20
CuPt-NC	1.5	250	560	-	S21
N, B-CNT	-	25	-	30 (~1.1 V)	S22

**Table S5.** Performance metrics of rechargeable Zn–air batteries based upon various electrocatalysts.

Catalyst	Recharge ability	Reference
PS-CNF	720 s/cycle for 600 cycles; 120 h	This work
NCNF-1000	600 s/cycle for 500 cycles; 83 h	S8
NPMC-1000	600 s/cycle for 600 cycles; 100 h	S9
P,S-CNS	720 s/cycle for 500 cycles; 100 h	S10
N-GRW	60 min/cycle for 150 cycles; 150 h	S11
NiO/CoN	10 min/cycle for 50 cycles; 8.3 h	S12
PCN-CFP	600 s/cycle for 50 cycles; 8.3 h	S13
LBSCFO-50	600 s/cycle for 100 cycles; 17 h	S23
NiO/Ni(OH) <sub>2</sub>	4200 s/cycle for 70 cycles; 83 h	S24
c-CoMn <sub>2</sub> /C	400 s/cycle for 155 cycles; 17 h	S25
NCNT/CoO-NiO-NiCo	600 s/cycle for 100 cycles; 17 h	S26
LaNiO <sub>3</sub> /N-CNT	600 s/cycle for 75 cycles; 12.5 h	S27
BNC	600 s/cycle for 66 cycles; 11 h	S28

## REFERENCES

- S1. S.S. Shinde, A. Sami, J. Lee, *Electrochim. Acta*, 2016, **214**, 173-181.
- S2. X. Zhang, X. Xie, H. Wang, J. Zhang, B. Pan, Y. Xie, *J. Am. Chem. Soc.*, 2013, **135**, 18-21.
- S3. J. Zhang, J. Sun, K. Maeda, K. Domen, P. Liu, M. Antonietti, X. Fu, X. Wang, *Energy Environ. Sci.*, 2011, **4**, 675-678.
- S4. Y. Zhang, T. Mori, J. Ye, M. Antonietti, *J. Am. Chem. Soc.*, 2010, **132**, 6294-6295.
- S5. S. Tonda, S. Kumar, S. Kandula, V. Shanker, *J. Mater. Chem. A*, 2014, **2**, 6772-6780
- S6. W. Zhang, H. Huang, F. Li, K. Deng, X. Wang, *J. Mater. Chem. A*, 2014, **2**, 19084-19094.
- S7. T. Ma, S. Dai, M. Jaroniec, S. Qiao, *Angew. Chem.*, 2014, **126**, 7409-7413.
- S8. Q. Liu, Y. Wang, L. Dai, J. Yao, *Adv. Mater.* 2016, **28**, 3000-3006.
- S9. J. Zhang, Z. Zhao, Z. Xia, L. Dai, *Nat. Nanotechnol.* 2015, **10**, 444-452.
- S10. S. Shinde, C.H. Lee, A. Sami, D. Kim, S.U. Lee, J.-H. Lee, *ACS Nano* 2017, **11**, 347-357.
- S11. H. Yang, J. Miao, S. Hung, J. Chen, H. Tao, X. Wang, L. Zhang, R. Chen, J. Gao, H. Chen, L. Dai, B. Liu, *Sci. Adv.* 2016, **2**, e1501122.
- S12. J. Yin, Y. Li, F. Lv, Q. Fan, Y. Zhao, Q. Zhang, W. Wang, F. Cheng, P. Xi, S. Guo, *ACS Nano* 2017, **11**, 2275-2283.
- S13. T. Ma, J. Ran, S. Dai, M. Jaroniec, S. Qiao, *Angew. Chem. Int. Ed.* 2015, **54**, 4646-4650.
- S14. S. Mao, Z. Wen, T. Huang, Y. Hou, J. Chen, *Energy Environ. Sci.* 2014, **7**, 609-616.
- S15. J. Wang, H. Wu, D. Gao, S. Miao, G. Wang, X. Bao, *Nano Energy* 2015, **13**, 387-396.
- S16. J. Masa, W. Xia, I. Sinev, A. Zhao, Z. Sun, S. Grützke, P. Weide, M. Muhler, W. Schuhmann, *Angew. Chem. Int. Ed.* 2014, **53**, 8508-8512.
- S17. G. Tian, M. Zhao, D. Yu, X. Kong, J. Huang, Q. Zhang, F. Wei, *Small* 2014, **10**, 2251-2259.
- S18. M. Prabu, K. Ketpang, S. Shanmugam, *Nanoscale*, 2014, **6**, 3173-3181.
- S19. Y. Li, M. Gong, Y. Liang, J. Feng, J. Kim, H. Wang, G. Hong, B. Zhang, H. Dai, *Nat. Commun.* 2013, **4**, 1805.
- S20. R. Cao, R. Thapa, H. Kim, X. Xu, M. Kim, Q. Li, N. Park, M. Liu, J. Cho, *Nat. Commun.* 2013, **4**, 2076.
- S21. V. Dhavale, S. Kurungot, *ACS Catal.* 2015, **5**, 1445-1452.

- S22. Y. Liu, S. Chen, X. Quan, H. Yu, H. Zhao, Y. Zhang, G. Chen, *J. Phys. Chem. C*, 2013, **117**, 14992–14998.
- S23. J. Jung, M. Risch, S. Park, M. Kim, G. Nam, H. Jeong, Y. Horn, J. Cho, *Energy Environ. Sci.*, 2016, **9**, 176-183.
- S24. D. Lee, J. Fu, M. Park, H. Liu, A. Kashkooli, Z. Chen, *Nano Lett.* 2016, **16**, 1794–1802.
- S25. C. Li, X. Han, F. Cheng, Y. Hu, C. Chen, J. Chen, *J. Nat. Commun.* 2015, **6**, 7345.
- S26. X. Liu, M. Park, M. Kim, S. Gupta, G. Wu, J. Cho, *Angew. Chem. Int. Ed.* 2015, **54**, 9654 –9658.
- S27. Z. Chen, A. Yu, D. Higgins, H. Li, H. Wang, Z. Chen, *Nano Lett.* 2012, **12**, 1946–1952.
- S28. X. Zhuang, D. Gehrig, N. Forler, H. Liang, M. Wagner, M. Hansen, F. Laquai, F. Zhang, X. Feng, *Adv. Mater.* 2015, **27**, 3789-3796.